A Study on the Asymmetric Rapid Intensification of Hurricane Earl (2010) Using the HWRF System

HUA CHEN

Rosenstiel School of Marine and Atmospheric Science, University of Miami, and NOAA/AOML/Hurricane Research Division, Miami, Florida

SUNDARARAMAN G. GOPALAKRISHNAN

NOAA/AOML/Hurricane Research Division, Miami, Florida

(Manuscript received 8 April 2014, in final form 17 October 2014)

ABSTRACT

In this study, the results of a forecast from the operational Hurricane Weather Research and Forecast (HWRF) system for Hurricane Earl (2010) are verified against observations and analyzed to understand the asymmetric rapid intensification of a storm in a sheared environment. The forecast verification shows that HWRF captured well Earl's observed evolution of intensity, convection asymmetry, wind field asymmetry, and vortex tilt in terms of magnitude and direction in the pre rapid and rapid intensification (RI) stages. Examination of the high-resolution forecast data reveals that the tilt was large at the RI onset and decreased quickly once RI commenced, suggesting that vertical alignment is the result instead of the trigger for RI. The RI onset is associated with the development of upper-level warming in the eye, which results from upper-level storm-relative flow advecting the warm air caused by subsidence warming in the upshear-left region toward the low-level storm center. This scenario does not occur until persistent convective bursts (CB) are concentrated in the downshear-left quadrant. The temperature budget calculation indicates that horizontal advection plays an important role in the development of upper-level warming in the early RI stage. The upper-level warming associated with the asymmetric intensification process occurs by means of the cooperative interaction of the convective-scale subsidence, resulting from CBs in favored regions and the shear-induced mesoscale subsidence. When CBs are concentrated in the downshear-left and upshear-left quadrants, the subsidence warming is maximized upshear and then advected toward the low-level storm center by the storm-relative flow at the upper level. Subsequently, the surface pressure falls and RI occurs.

1. Introduction

Predicting the rapid intensification (RI) of tropical cyclones (TCs) is a complex, challenging, and important forecast problem. The difficulty of forecasting RI stems from a lack of understanding of the physical mechanisms that are responsible for these events (Kaplan and DeMaria 2003; Kaplan et al. 2010). In general, apart from the well-documented impacts of upper ocean on intensity changes (e.g., Byers 1944; Black 1983; Shay et al. 2000), environmental factors such as wind shear (e.g., Gray 1968; Merrill 1988; DeMaria and Kaplan 1994), moisture in the low to mid troposphere (e.g., Gray 1968), and inner-core processes ranging from convective to mesoscale (e.g., Schubert and Hack 1982; Willoughby et al. 1982; Kossin and Schubert 2001; Eastin et al. 2005a,b) all have been known to influence the RI of TCs. All these factors interact in a nonlinear fashion, making the RI problem a complex forecast issue. Although there is currently much less skill in forecasting RI with fidelity (Cangialosi and Franklin 2012), cloud-resolving numerical models using a horizontal grid resolution of 1–3 km have demonstrated the capability to capture the relevant processes. For instance, several recent studies have shown that vortical thermal plumes and the subsequent development of the warm core is one possible pathway for RI of at least an initially symmetric vortex (e.g., Hendricks et al. 2004; Montgomery et al. 2006; Van Sang et al. 2008; Gopalakrishnan et al. 2011; Chen and

Corresponding author address: Dr. Sundararaman G. Gopalakrishnan, NOAA/AOML/ Hurricane Research Division, 4301 Rickenbacker Causeway, Miami, FL 33149.
E-mail: gopal@noaa.gov

DOI: 10.1175/JAS-D-14-0097.1

Zhang 2013). Indeed, recent observational studies (Harnos and Nesbitt 2011; Jiang 2012; Kieper and Jiang 2012; Rogers et al. 2013) also support the fact that the majority of RI cases are characterized by a symmetric ring of precipitation prior to RI onset. However, in the presence of vertical wind shear (VWS), which typically occurs in the tropical atmosphere, storms have also been observed to rapidly intensify (Molinari et al. 2006; Molinari and Vollaro 2010). Yet such RI cases have received little attention. This may be due to the lack of routine high-resolution observations in space and time needed to support both the analysis of the convective-scale and mesoscale dynamical processes within storm-core regions and verification of the model-based simulations.

In this study, we analyze the thermodynamic processes associated with RI under the influence of VWS for the case of Hurricane Earl (2010). The study capitalizes on the availability of a multiday sequence of high-resolution observations collected during the National Oceanic and Atmospheric Administration's (NOAA) hurricane field program campaign (Rogers et al. 2012; Montgomery et al. 2014) and the high-resolution forecast from the Hurricane Weather Research and Forecasting (HWRF) system that verified well in terms of track and intensity, as well as storm structure evolution, against available observations. The high skill of the forecast provides the basis for confidence in the forecast model representation of the relevant processes analyzed in this study.

Several prior studies on the intensification of TCs have indicated that the development and enhancement of the warm core is a necessary condition for intensification. In a series of idealized HWRF simulations in a shear-free environment, Gopalakrishnan et al. (2011) showed that rapid warming of the core was closely associated with the development of organized, moist, vortical thermal plumes around the eyewall region. This study related warm core formation to a wind-induced surface heat exchange type of feedback (Emanuel 2003) in the hurricane boundary layer, wherein the surface pressure decreased (by hydrostatic principles), resulting in an increase in wind speed and surface enthalpy fluxes (θ_e) and, subsequently, a warmer core. In a study of Hurricane Wilma (2005) (Chen et al. 2011; Zhang and Chen 2012; Chen and Zhang 2013), the authors showed that an upper-level (i.e., $z = 14$ km) warm core formed, in coincidence with the RI onset, as a result of the descent of stratospheric air in the presence of weak, storm-relative flows aloft. The descent of stratospheric air resulted from the upper-level detrainment of convective bursts (CBs) occurring in the vicinity of the radius of maximum wind (RMW), where higher-θ_e air was located. The associated subsidence warming did not become effective until an organized upper-level outflow was established with a weak cyclonic circulation and decreased static stability in the eye. Several other studies also linked CBs with storm intensification (e.g., Steranka et al. 1986; Rodgers et al. 1998; Heymsfield et al. 2001; Guimond et al. 2010).

However, unlike the development of an axisymmetric vortex in an idealized, shear-free environment or the conducive large-scale environment in which Hurricane Wilma (2005) underwent an explosive intensification, a sheared environment (especially when the 850–200-hPa average shear is $\geq 5\,\mathrm{m\,s^{-1}}$) is generally considered hostile to a developing TC and is likely to inhibit any rapid deepening mainly because of vortex tilt (Kaplan and DeMaria 2003; Kaplan et al. 2010). Nevertheless, there are a few examples of TCs observed to have undergone RI in such a hostile environment. For instance, the surface pressure of Tropical Storm Gabrielle (2001) dropped 22 hPa in 3 h when the environmental deep layer shear was $13\,\mathrm{m\,s^{-1}}$. Molinari et al. (2006) and Molinari and Vollaro (2010) reported some unprecedented findings from this case. These studies revealed that the RI of Gabrielle occurred when one intense convective cell that developed in the downshear left, where almost all radar return was located, moved cyclonically and inward to the 17-km radius, which was within the RMW and enhanced the efficiency for kinetic energy production. Another well-documented case is Hurricane Guillermo (1997) (Eastin et al. 2005b; Reasor et al. 2009; Sitkowski and Barnes 2009; Reasor and Eastin 2012). Eastin et al. (2005b) used extensive airborne radar, dropwindsonde, and flight-level observations to illustrate typical azimuthal distribution of buoyant convection associated with VWS. They found that mesoscale vertical motions exhibited a wavenumber-1 structure with maximum ascent downshear and weak descent upshear, with the downdraft core located upshear next to downshear deep convection. Reasor et al. (2009) demonstrated that the greatest intensification during the 6-h Doppler observation period coincided with the formation and cyclonic rotation of several particularly strong CBs through the left-of-shear semicircle of the eyewall when the deep layer shear was $7–8\,\mathrm{m\,s^{-1}}$. The composite study of Corbosiero and Molinari (2002, 2003) used 35 Atlantic basin TCs from 1985–99 while they were over land and within 400 km of the coast over water. The authors discovered a strong correlation existed between the azimuthal distribution of lightning flashes and VWS in the environment, especially when the VWS exceeded $5\,\mathrm{m\,s^{-1}}$.

Theoretical studies (Hack and Schubert 1986; Vigh and Schubert 2009) using the Eliassen–Sawyer equation have demonstrated that diabatic heating located inside the RMW is more efficient in intensifying the vortex. This conclusion was confirmed by a numerical study that

explored the intensification of a balanced, baroclinic, tropical cyclone–like vortex in which convection was displaced from the vortex center (Nolan et al. 2007). The result from a case study of Hurricane Gabrielle (Molinari and Vollaro 2010) confirmed this conclusion also. In a composite of airborne Doppler data from multiple storms that were either intensifying or remaining steady-state, Rogers et al. (2013) showed that the radial location of the peak of the distribution of CBs was within the RMW for intensifying storms, whereas it was outside the RMW for steady-state storms. In an idealized study of the impact of shear on TC vortex intensification, Chen and Fang (2012) showed that weak shear-induced downshear deep convection within the RMW because of small tilt and tended to facilitate TC intensification. In contrast, deep convection outside the RMW due to large vortex tilt in strong shear cases tended to curb TC intensification.

Other than the importance of the radial location of diabatic heating, a few studies have shown that the vortex tilt direction is crucial also for vortex intensification in a sheared environment. Using a dry adiabatic model, Reasor et al. (2004) demonstrated that TC-like vortices achieved approximate steady-state tilts to the left of the shear vector. In a real tropical environment, the vortex tilt is usually more related to the location and timing of the deep convection. Indeed, in idealized experiments using a cloud-resolving model, Zhang and Tao (2013) showed that vortex tilt was determined by the location of organized deep convection. Both the vertical tilt of the vortex and the effective (local) VWS decreased considerably after the tilt angle reached 90° to the left of the environmental shear, and the TCs intensified immediately afterward.

It should be noted that all of the above studies were either restricted to an observational analysis or dealt with a highly idealized environment that, at best, might provide insight on some aspect of the TC intensification process. The current work and associated publications are expected to bridge the gap between existing theoretical studies and findings from observations specifically related to the rapid development of an initially asymmetric TC vortex in a sheared environment. The next section describes the model configuration of the operational HWRF. Section 3 provides a brief overview of the RI of Hurricane Earl. Section 4 presents verification of the model-predicted storm structures against various observations. Section 5 shows some model-predicted, inner-core structures and structural changes during Earl's pre-RI and RI stages. Section 6 demonstrates the formation of an upper-level warm core that is associated with the RI of Earl. Section 7 explains why the RI occurs at that specific time. A summary and some concluding remarks are given in the final section.

2. The HWRF Model, configuration, and physics

The triply-nested, cloud-resolving version of the atmosphere–ocean coupled operational HWRF system jointly developed by NOAA's National Weather Service/National Centers for Environmental Prediction (NWS/NCEP) and the Hurricane Research Division (HRD) of the Atlantic Oceanographic and Meteorological Laboratory under the auspices of the Hurricane Forecast Improvement Project was used in this study (Gopalakrishnan et al. 2011, 2012, 2013; Tallapragada et al. 2014). In brief, this version has a number of important physics upgrades, consisting of modifications to the NCEP Global Forecasting System (GFS) planetary boundary layer (PBL) based on observational findings (Gopalakrishnan et al. 2012; Zhang et al. 2013), improved Geophysical Fluid Dynamics Laboratory (GFDL) surface physics, improved Ferrier microphysics (Ferrier 1994), and implementation of the new GFS shallow convective parameterization (Hong and Pan 1996). In this coupled model simulation, the Princeton Ocean Model adapted for TCs (POM-TC; Yablonsky and Ginis 2008), which was developed at the University of Rhode Island, is used for providing sea surface temperature (SST). More details on the model parameterization schemes may be found in the above-mentioned references.

HWRF uses a model-consistent vortex from the previous cycle that has been relocated and adjusted toward current pressure and wind observations (Liu et al. 2006; Tallapragada et al. 2014). This study uses output from the 1800 UTC 26 August 2010 retrospective forecast, with vortex initialization and assimilation consisting of three major steps: 1) interpolation of the global analysis fields from the GFS onto the operational 27–9–3-km model grids; 2) removal of the GFS vortex from the global analysis; and 3) addition of the HWRF vortex modified from the previous cycle's 6-h forecast based on observed location and strength. The improved prediction of the HWRF system is partly attributed to the surface and boundary layer combination being reconstructed on the basis of hurricane observations and the advanced initialization procedure (Tallapragada et al. 2014; Goldenberg et al. 2014, manuscript submitted to *Wea. Forecasting*). For instance, forecast errors from the HWRF system for Earl were generally low, and those from the particular cycle used here were exceptional, as will be demonstrated in section 4. There were a few other cycles that could have been used; however, the current cycle captured the RI phase starting at 48 h into the forecast so that any lack of realism related to initial conditions and subsequent spinup could be avoided.

3. Overview of the RI of Hurricane Earl

A detailed account of Hurricane Earl is reported in Cangialosi (2010). In summary, the hurricane originated from a tropical easterly wave and organized into a tropical depression by 0600 UTC 25 August after acquiring sufficient convective organization when centered about 370 km west–southwest of the Cape Verde Islands. As convection became better organized, the system strengthened into a tropical storm by 1200 UTC 25 August and became a hurricane at 1200 UTC 29 August in an environment with warm SSTs of 28°–29°C and moderate VWS. The hurricane underwent RI with a 21 m s^{-1} increase in wind speed over 24 h, becoming a category 4 hurricane by 1800 UTC 30 August as it slowed and gradually turned northwestward. In this work, we focus on the pre-RI and early RI forecasts (i.e., 1800 UTC 26 August–1800 UTC 29 August).

4. Model verification

Figure 1 depicts the time evolution of Hurricane Earl in terms of track, central pressure, maximum 10-m wind, and the RMW.[1] Figure 1a shows the track of the storm from the HWRF forecast (red line) compared with the best-track analysis (black line) plotted at a 6-h interval for the period of 1800 UTC 26 August to 1800 UTC 31 August. As can be seen, the predicted track follows the observations reasonably well, in general, and 95% of Earl's track errors are caused by the translation speed difference, with the predicted hurricane moving slower than the observed hurricane. The track errors at 24, 48, and 72 h, critical for understanding the modeled intensification process, are 104, 177, and 181 km, respectively, and these numbers compare favorably to the season's best-track estimates of 104, 171, and 248 km for the same period (Cangialosi and Franklin 2011).

Figure 1b, which shows a time series of the central pressure from the HWRF (blue line) and best-track analysis (black line), indicates that the HWRF forecast reasonably reproduced the central pressure change, particularly for the pre-RI and RI periods. Further examination of the pressure field shows there is a clear semidiurnal oscillation with 1.5-hPa amplitude. To obtain a clear signal that is related only to the storm itself, a filter with 1.5-hPa amplitude and 12-h period was applied to the time series of central pressure (blue line), and the filtered time series of central pressure is depicted in the red line. It captured the pre-RI stage, during which pressure remained almost unchanged in the first 27 h and deepened slightly between 27 and 52 h. The continuous steady deepening period began at 52 h. While the deepening rate between 52 and 57 h was only 0.1 hPa h^{-1}, the deepening rate increased rapidly after 57 h, denoting RI onset for the HWRF forecast. Based on the maximum 10-m wind speed at 24, 48, and 72 h, the intensity errors were 0.8, 1, and 5 m s^{-1}, respectively, which are extremely good values when compared with the 2010 season intensity forecast errors of 6.5, 10.2, and 8.6 m s^{-1} (Cangialosi and Franklin 2011).

Figure 1c compares the time series of the RMW from the HWRF forecast and the observations. As can be seen, the RMW from the HWRF forecast is about 70 km smaller than the observations at the initial time, which is likely a result of cycling of the vortex from the previous run. It should be noted that while the vortex from the cycled runs was adjusted toward the observed central pressure (maximum 10-m wind speed) and radius of 17 m s^{-1} wind from the best-track data, no initial adjustment for the RMW was performed in this initialization scheme. Nevertheless, after 24 h into the forecast, the RMW from HWRF is comparable to the observations, reaching about 110 km. Both the observed and simulated RMWs contract rapidly between 24–36 h. The contraction in the HWRF forecast with 2-min resolution is realized through a series of significant fluctuations that may not be captured from the 6-h best track. The RMW for both the observations and HWRF forecast remains nearly constant between 36 and 60 h, with a slight contraction around 45 h. A large contraction in the RMW occurs after 60 h. The modeled RMW contracts from a radius of about 50 to 20–30 km, consistent with the observations. The model verification in Fig. 1 shows that the HWRF forecast reproduces the intensity and storm size exceptionally well for this cycle, making it an excellent case to provide further forecast insights on the intensification problem. Yet one question remains: Is this good forecast because of the right reasons? To answer this question, the forecasted environment and storm structure verifications will be examined first.

Figure 2 provides the mean large-scale environment from the HWRF forecast and GFS analysis in terms of VWS and SSTs. Although direct comparison of point value of shear and SSTs between low-resolution GFS analysis and a high-resolution ocean-coupled HWRF system may be misleading, we use these comparisons to verify only the trend. As can be observed in Fig. 2a, both the HWRF shear (red line) and GFS shear (black line) show some oscillations around 5 m s^{-1}, and they are generally in phase with the amplitude of GFS shear about 2 m s^{-1} larger than that of HWRF shear. It is

[1] It should be noted that the outputs from the model were plotted at higher frequency (i.e., 2 min) for further analysis. However, the observations are plotted at a 6-h interval and only provide a scale of measure of the model performance in terms of its overall behavior.

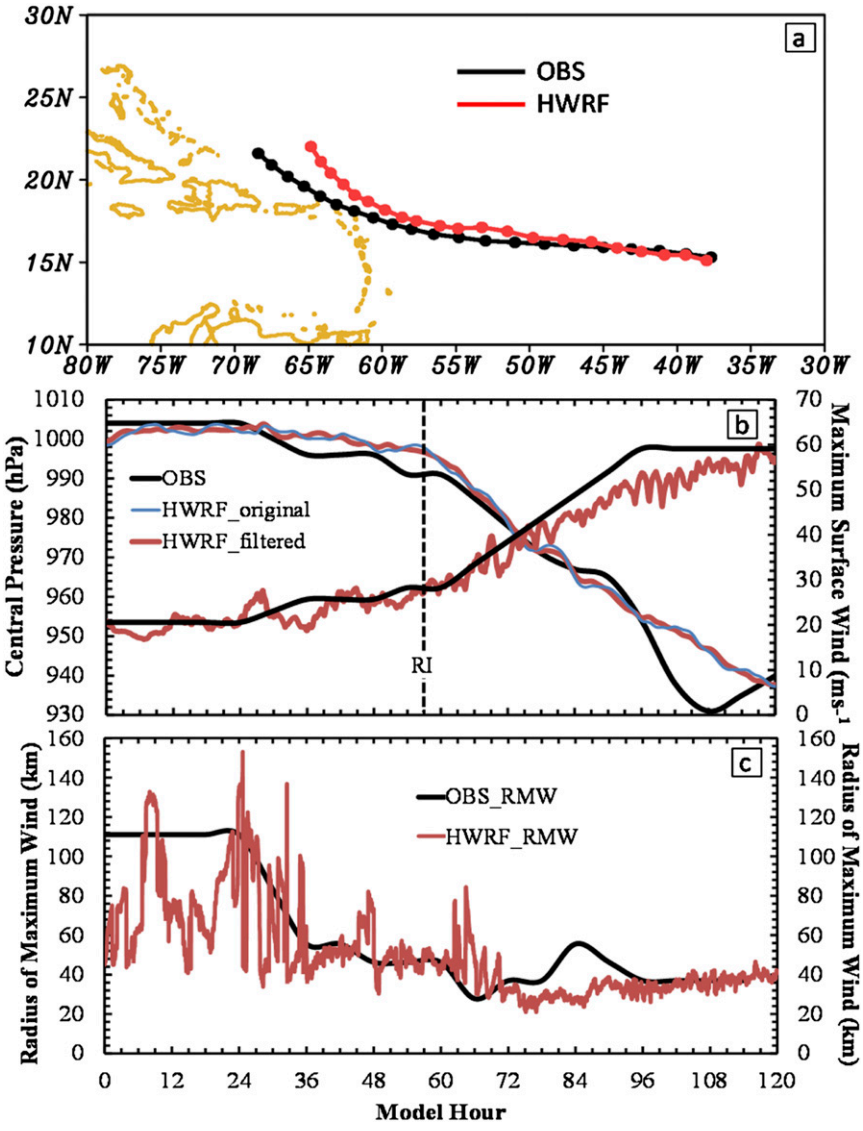

FIG. 1. (a) HWRF-forecasted (red line) and observed track (black line) at 6-h intervals; (b) time series of HWRF-forecasted (2-min resolution; red line) and observed (6-h resolution; black line) maximum surface wind (V_{max}, m s^{-1}) and central pressure (P_{min}, hPa) for the period from 1800 UTC 26 Aug to 1800 31 UTC Aug. For HWRF-forecasted pressure, a semidiurnal filter is applied to the central pressure time series (blue line) to remove storm-unrelated pressure change and red line shows the filtered central pressure. The vertical black dashed line indicates RI onset. (c) Time series of HWRF-forecasted (2-min resolution; red line) and observed (6-h resolution; black line) RMW (km).

noteworthy that shear increases a few hours prior to RI and in the early RI stage for the HWRF forecast. As for the GFS analysis, shear also increases in the first 6 h of RI. Apparently, RI onset, at least in this case, is not caused by decreasing shear, as postulated in earlier studies. Such studies suggested that shear curbs storm intensification through a number of pathways, including ventilation of the upper-level warm core (Frank and Ritchie 2001), middle-level ventilation that reduces the Carnot engine efficiency (Tang and Emanuel 2010), and reduced temperature in the boundary layer inflow (Riemer et al. 2010). Figure 2b shows that SSTs increase drastically in the pre-RI stage in both the HWRF forecast and GFS analysis. As the storm approaches RI, the HWRF forecast SSTs almost level off, but the GFS SSTs continue increasing to 66 h. Nevertheless, the general trend is very similar, and the GFS SSTs are slightly warmer than the HWRF SSTs after RI onset. In this

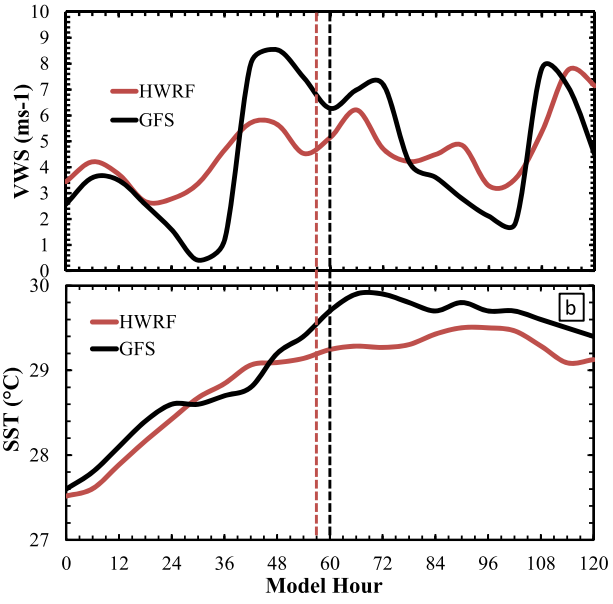

FIG. 2. Time series of (a) vertical wind shear between 850 and 200 hPa averaged within 1000 km × 1000 km and (b) SSTs at the storm center for the HWRF forecast (red line) and GFS reanalysis (black line). The black and red vertical dashed lines indicate RI onset for observation and HWRF forecast, respectively.

case, both the shear and SSTs imply that the role of environmental factors in controlling the RI of Earl is not clear cut, providing a great example to study how multiscale interaction leads to the RI of Earl.

Figure 3 compares radar reflectivity from the HWRF forecast at flight level (3-km altitude) against the lower fuselage radar observations available in the HRD database (http://www.aoml.noaa.gov/hrd/Storm_pages/earl2010/radar.html) for the pre-RI and RI stages. It should be emphasized that a one-on-one comparison may sometime be misleading in regions of weak echoes due to sea clutter (Marks 1985). Nevertheless, in general, the convective asymmetry, which is governed by environmental shear, is also reproduced in the HWRF forecast. As can be seen, in the pre-RI stage when shear is northerly, the inner core is highly asymmetric, with deep convection occurring roughly downshear and downshear-left in both the observed reflectivity and the HWRF forecast reflectivity. The magnitude of the northerly shear at this time is about 7.7 and 5.1 m s^{-1}, respectively, for the GFS analysis and HWRF forecast. Most of the deep convection falls outside the 50-km radius for both the observations and HWRF forecast. After Earl begins RI, the shear remains northerly, and the reflectivity for both the observations and HWRF forecast is still highly asymmetric. Deep convection occurs downshear left in the inner core and upshear in an outer rainband, which is located at a larger radii in HWRF forecast than the observations. Although much of the high reflectivity due to convection falls outside the RMW for both the observations and the HWRF forecast, there is a significant amount of convection near the center (i.e., inside the 50-km radius), which is expected to have a higher efficiency in intensifying the vortex, as demonstrated in previous studies (Hack and Schubert 1986; Nolan et al. 2007; Vigh and Schubert 2009; Rogers et al. 2013).

Other than the wavenumber-1 asymmetry in the horizontal distribution of reflectivity, another major response of the storm structure to shear is vortex tilt with altitude. Figure 4 compares the tilt[2] from the HWRF forecast against the observations in the pre-RI and RI stages. As shown in Fig. 4a, the observed tilt (measured by the circulation displacement between 2 and 8 km) is toward the southeast in the pre-RI stage with 75-km magnitude, while the corresponding RMW at the surface is only about 50 km. According to Chen and Fang (2012), such a tilt–RMW configuration will lead to the deep convection falling outside of the RMW, and, subsequently, the diabatic heating efficiency should be significantly diminished. However, a major concern about using the surface RMW in evaluating the efficiency of diabatic heating is that the maximum diabatic heating usually occurs in the middle and upper levels. For a highly sloped eyewall, the surface RMW might be significantly different from the RMW at the upper level. For this reason, a fixed radius was used instead of the surface RMW to evaluate the efficiency of diabatic heating. The wavenumber-1 asymmetry in the low-level wind field has the maximum wind speed located in the northeast quadrant (shaded) as a result of the northwestward translation of the storm. The wind field asymmetry and the vortex tilt from the HWRF forecast (Fig. 4b) resemble the Doppler-observed structure very well. The tilt in the RI stage (i.e., 9 h after RI onset) rotates anticyclonically and becomes much smaller for both the observations and HWRF forecast. The shear, 6.0–6.5 m s^{-1} at this time, is greater than the shear in the later time of the pre-RI period for the HWRF forecast, suggesting the tilt magnitude is more likely determined by the ratio of shear to storm intensity, instead of the shear magnitude alone. For a given amount of shear, a weaker storm will respond with larger tilt, while a stronger storm will be more resilient to the shear and exhibit less tilt.

5. Storm structure evolution

Figure 4 shows that tilt is large in the pre-RI stage and reduces during the RI stage. Previous studies have

[2] For the purpose of comparison with observations, we have computed the tilt using Earth-relative flow in this section.

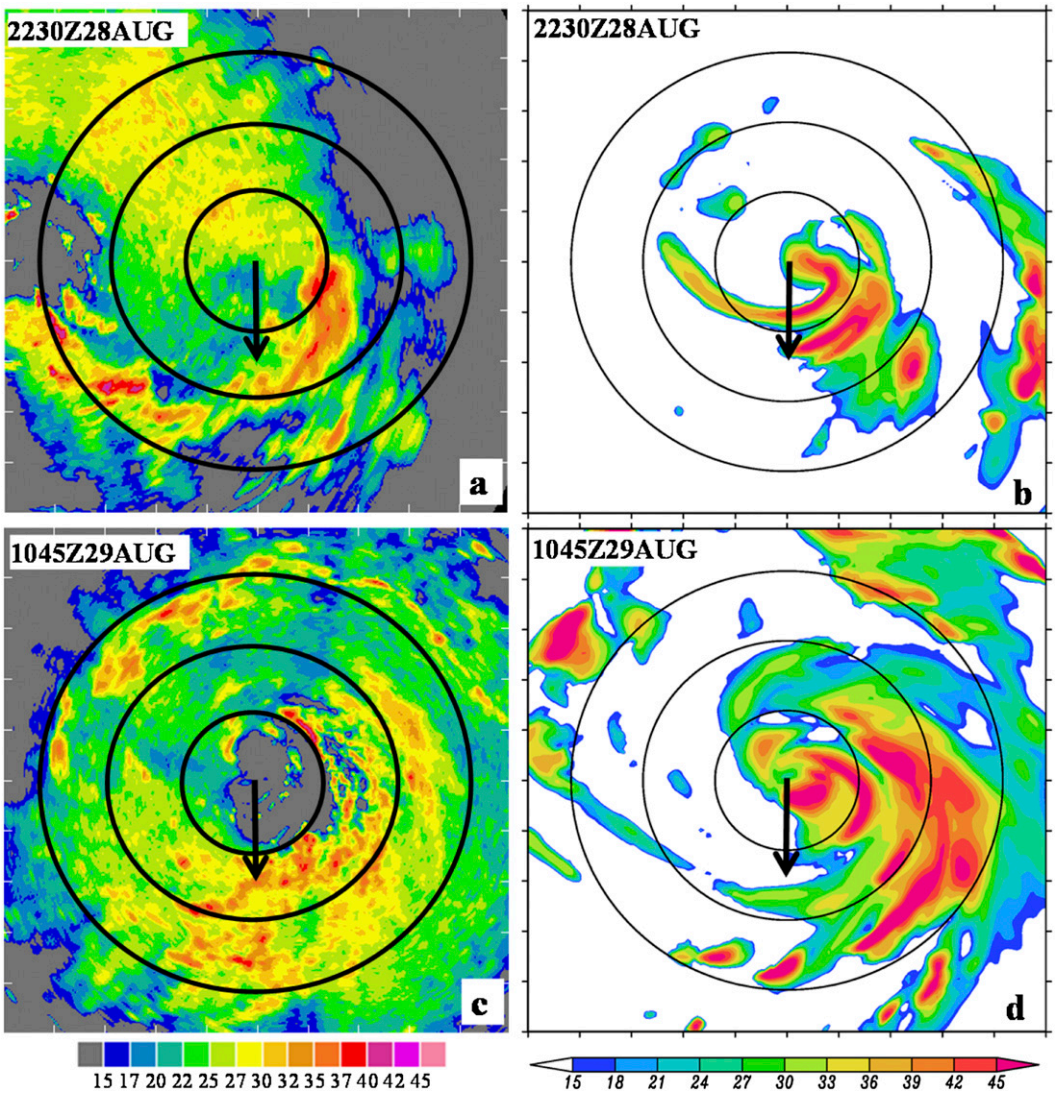

FIG. 3. (a),(c) Lower fuselage radar observation of radar reflectivity at 2230 UTC 28 Aug and 1045 UTC 29 Aug, respectively. (b),(d) HWRF-forecasted radar reflectivity from the 29.5-h forecast (valid at 2330 UTC 28 Aug) and the 62.75-h forecast (valid at 0845 UTC 29 Aug), respectively. The black circles indicate the 50-, 100-, and 150-km radii, and the black arrow indicates the shear direction. Ticks on the axes are at a 36-km interval.

shown that RI onset is associated with a vertical alignment of the vortex (e.g., Chen 2012). To examine if vortex alignment is the trigger for the RI of Hurricane Earl, the hourly tilt hodograph from 48 h (i.e., 9 h prior to RI onset) to 66 h (i.e., 9 h after RI onset) is depicted in Fig. 5. The tilt is northeastward at 48 h with 41-km magnitude, rotating clockwise to the south as its magnitude shrinks significantly to 22 km at 51 h. The tilt vector then rotates cyclonically, while its magnitude increases to 50 km at 57 h when RI commences. It continues to rotate cyclonically, but magnitude rapidly decreases after 58 h. Within this 18-h period, the minimum tilt is 10 km, which occurs at 65 h (i.e., 8 h after RI onset). In general, the tilt decreases with intensification, as shown in Figs. 4 and 5, but the tilt at RI onset (i.e., t = 57 h) is still large. The tilt precession shown in Fig. 5 demonstrates that vertical alignment might be the result instead of the trigger for RI. Nevertheless, Earl does become better aligned in the later RI stage despite its highly asymmetric convective distribution.

6. The upper-level warming

The accelerated deepening of central pressure is associated with a rapid temperature change in the eye center caused by either an abrupt increase in magnitude,

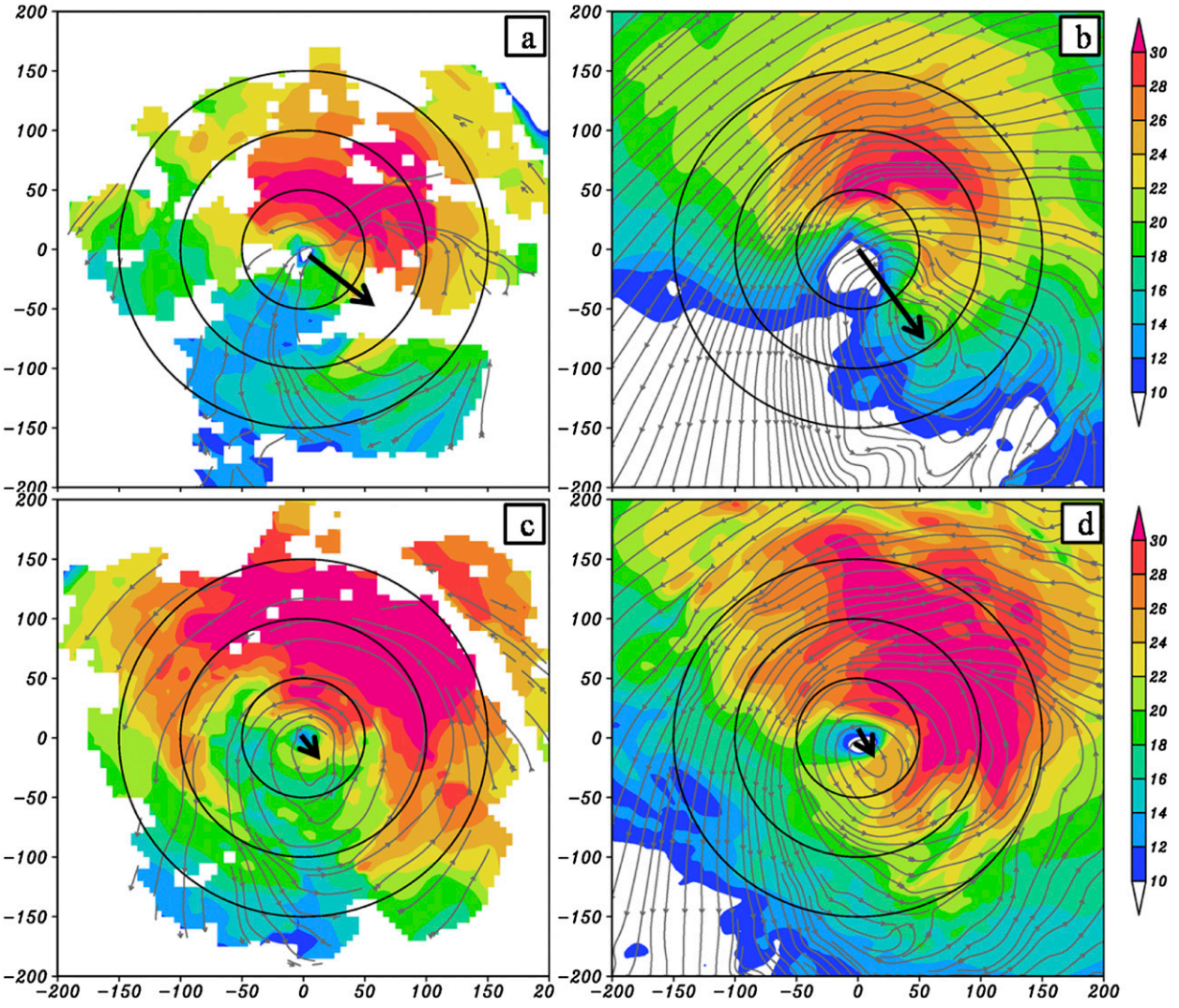

FIG. 4. Horizontal cross section of wind speed (color shading, m s^{-1}) at 2-km altitude and streamlines (gray lines with arrowheads) at 8-km altitude from (a),(b) composite radar observation in the pre-RI and RI stage, respectively. (b),(d) HWRF forecast in the pre-RI and RI stage, respectively. The black circles indicate the 50-, 100-, and 150-km radii, and the black arrows indicate the tilt direction.

as demonstrated in the idealized numerical study of Gopalakrishnan et al. (2011), or by a sudden elevation of the warm-core height. Chen and Zhang (2013) showed that the RI onset of Hurricane Wilma (2005) was associated with the warm core being elevated from 12- to 14-km altitude; however, in those studies, this did not occur until the vortex became horizontally symmetric and vertically aligned.

To examine if Earl's RI occurred as a result of the warm core shifting upward, despite its significant horizontal asymmetry and vertical tilt, the time–height cross section of temperature perturbation with respect to the 400 km × 400 km domain-averaged temperature profile at forecast initial time is plotted in Fig. 6a. As observed, there is a stark difference between the pre-RI and RI stages, similar to what is shown in Zhang and Chen (2012). The warming is focused below 8 km in the pre-RI stage and then suddenly extends to 14 km in the RI stage, with maximum warming setting in at 8-km altitude at the end of the forecast.

To quantify the contribution of the warming above 8 km to the surface pressure change, a hydrostatic calculation is performed by removing the warming above 8 km, and the result is plotted in Fig. 6b. The original surface pressure is also plotted for the purpose of comparison. It can be seen that RI would not have occurred and that the final central pressure would have been 45 hPa higher without the warming above 8 km. This figure clearly demonstrates that the RI of Earl is associated with warming in the upper level (i.e., above 8 km).

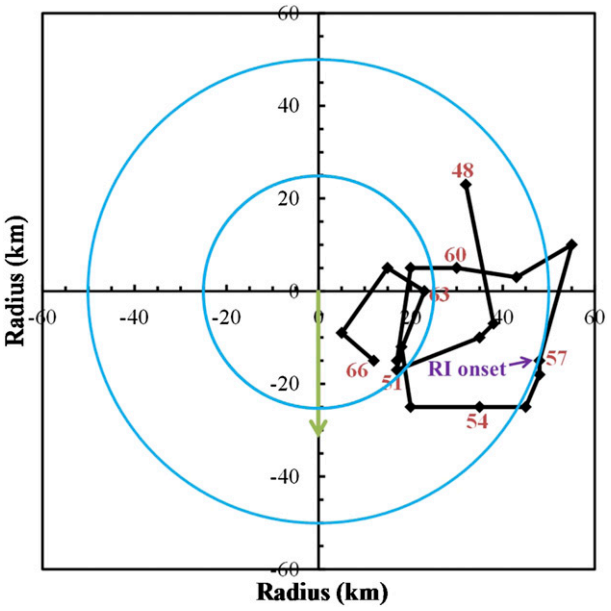

FIG. 5. Hourly hodograph of tilt from 48 to 66 h. The blue circles depict the 50- and 100-km radii and the downward green arrow shows the northerly shear. Represented is the mean RMW and shear direction within this 18-h period. The tilt is calculated as the horizontal displacement of storm-relative circulation centers between 2- and 8-km altitude.

One question spontaneously arises: What causes the warming above 8 km? Zhang and Chen (2012) explained that the upper-level warming development in Hurricane Wilma (2005) was due to compensating subsidence from CBs trapped in the inner-core region because of weak, storm-relative flow in the eye and large inertial stability associated with the development of the symmetric eyewall. However, Hurricane Earl never achieved a fully symmetric eyewall in this 120-h forecast, and there is northerly flow across the storm center at 8-km altitude, as shown in Fig. 5 at 60 h. Apparently, the development of upper-level warming in Earl was very different from that in Hurricane Wilma.

Previous studies (Nolan et al. 2007; Vigh and Schubert 2009; Rogers et al. 2013, 2015) have already pointed out that CBs taking place inside the RMW are more efficient in spinning up the vortex. To test this hypothesis, a time series of CB[3] numbers in the first 72 h stratified by the radius (i.e., $r \leq 50$ km, $50 \leq r \leq 100$ km, $100 \leq r \leq 150$ km, and $150 \leq r \leq 200$ km) is shown in Fig. 7a. Fixed radii are used instead of the RMW, because the RMW as shown in Fig. 1c exhibits large fluctuations, especially in the early hours of the forecast. Time series of shear magnitude, central pressure, and maximum surface wind are also plotted in Fig. 7a to facilitate viewing the relationship between them and CB activity. While CBs inside 50 km are considered as being in a favorable region for intensifying the vortex, most CBs fall within the 50–150-km radius. In general, the number of CBs at all radii exhibit episodic behavior at irregular intervals.

Nguyen et al. (2011) pointed out that convective available potential energy (CAPE) in the storm environment needed to be restored to support a new CB episode after a previous CB episode exhausted the CAPE. There are three major episodes in the pre-RI stage (i.e., prior to 57 h): 9–15, 24–30, and 36–42 h. The first two episodes occur when the shear magnitude is $<4\,\mathrm{m\,s^{-1}}$, and the third episode occurs when the shear increases to near $6\,\mathrm{m\,s^{-1}}$. Figure 7a shows that the surface wind speeds respond to each episode with dramatic fluctuations, increasing rapidly when the CB episode starts picking up and weakening quickly when the episode starts to die down. In the second episode, the surface wind speed increases from 20 to $28\,\mathrm{m\,s^{-1}}$ from 24 to 27 h, then rapidly returns to its pre-episode value at the end of the episode. However, at the end of the third episode, there is a net $3\,\mathrm{m\,s^{-1}}$ increase in the wind speed. Starting at 53 h, the surface wind speed shows a steady increase, with small fluctuations as the shear increases from 5 to $6.8\,\mathrm{m\,s^{-1}}$. In contrast to the surface wind response to the CB episodes, central pressure does not show a similar response, yet it does begin to deepen continuously after 52 h (i.e., 1 h prior to the surface wind increases).

Based on this finescale analysis of the time series of central pressure and surface wind, it seems the RI onset should be flagged at 52 or 53 h. However, as pointed out in section 4, the deepening rate is still only about $0.1\,\mathrm{hPa\,h^{-1}}$ around this time. Nevertheless, the 52–57-h time period into the forecast can be viewed as a preconditioning stage for RI. How the preconditioning process occurs is not yet clear in Fig. 7a. The evolution of CBs occurring near the center (i.e., ≤50-km radius) does not appear to be closely related to intensity change, which implies diabatic heating alone close to the center is an insufficient condition for RI in the case of Earl.

To examine the possible relationship between CB azimuthal distribution and intensity change, Fig. 7b shows a similar time series to Fig. 7a, but the CBs are stratified by the shear-oriented quadrants instead of the radius. The evolution of CBs in Fig. 7b is very similar to Fig. 7a before 50 h, and periodic CB episodes occur randomly in different quadrants. However, CBs in the downshear-left (red line) dominate after 50 h, and this downshear-left dominance pattern persists until 72 h. The central pressure and surface wind speed start to

[3] A convective burst is defined as a grid point with its maximum vertical motion $> 3\,\mathrm{m\,s^{-1}}$ in the column.

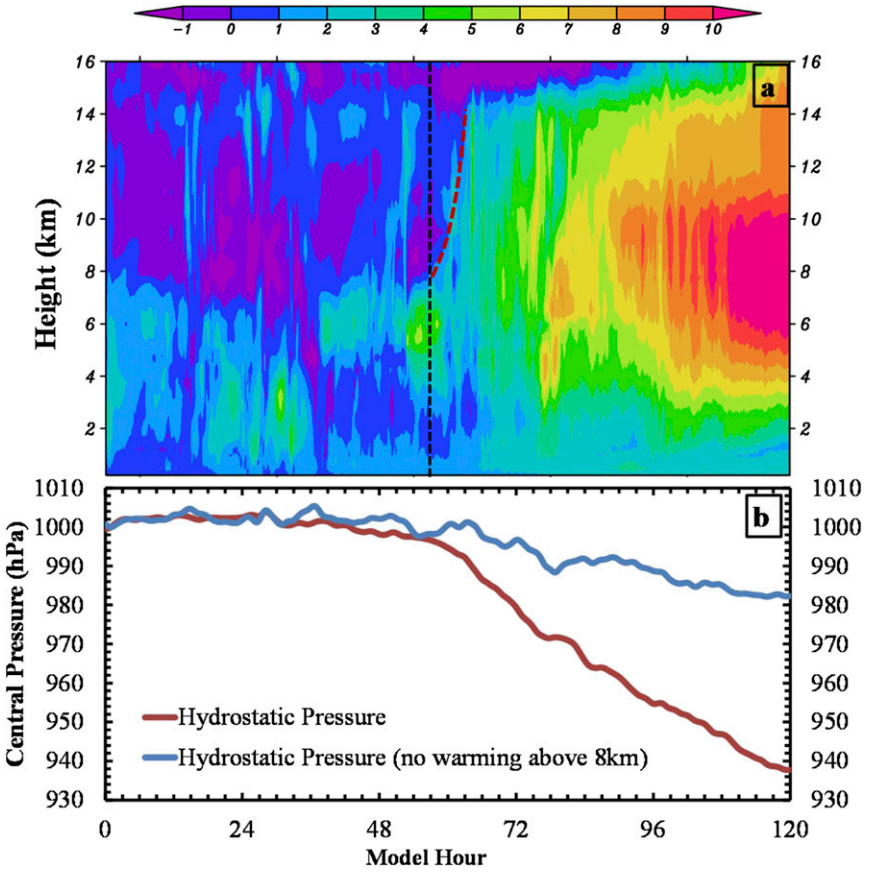

FIG. 6. (a) Time–height cross section of temperature perturbation at the eye center of Earl with respect to the reference temperature profile defined as the 400 km × 400 km area-averaged mean temperature at the model initial time. The vertical black dashed line indicates RI onset and the red dashed line shows the trend of the warm-core boundary. (b) Time series of central pressure from the whole column warming (red line) and the only the warming below 8 km (blue line).

intensify continuously a couple of hours after the downshear-left dominance pattern occurs, which indicates downshear left is a favorable quadrant for CBs to intensify the storm. Downshear-left CB episodes occur prior to 50 h, but there are two major differences between those episodes and the episode after 50 h. First, there are many other CBs taking place in other quadrants, which make downshear-left CBs much less distinct. This suggests downshear-left dominance of CB distribution might be one of the necessary conditions for the RI of Earl. Second, the duration of downshear-left CBs is shorter than the episode after 50 h, which suggests the persistence of CBs is also important, consistent with previous studies (e.g., Nolan et al. 2007).

The CB distribution is further refined by shear-oriented quadrants within a 50-km radius to consider both the radius and azimuthal factors. As shown Fig. 7c, there are two distinct episodes in the downshear-left quadrant, with the second episode dominating over all other quadrants, although its duration is shorter than that in Fig. 7b. Figure 7c suggests that both the radius and shear-oriented direction are important in determining the efficiency of CBs to spin up the vortex.

Figure 7 shows that there is a relationship between CB activity and intensity change, especially when the CBs are measured in shear-oriented quadrants. But exactly how are they related? As shown in Fig. 6a, RI onset is related to sudden warming in the upper troposphere of the eye center. Subsidence in the hurricane eye is well recognized as the mechanism responsible for the formation of the warm core, but such a mechanism has remained enigmatic, since this branch of circulation consumes energy produced elsewhere in the hurricane (Willoughby 1998). Previous studies have put forward a few hypotheses. Using an axisymmetric vortex model, Smith (1980) demonstrated that subsidence warming in the eye was mechanically driven by decreasing tangential winds in the vertical as a consequence of thermal wind balance. Willoughby (1998) viewed subsidence as the result of RMW contraction as the storm intensified.

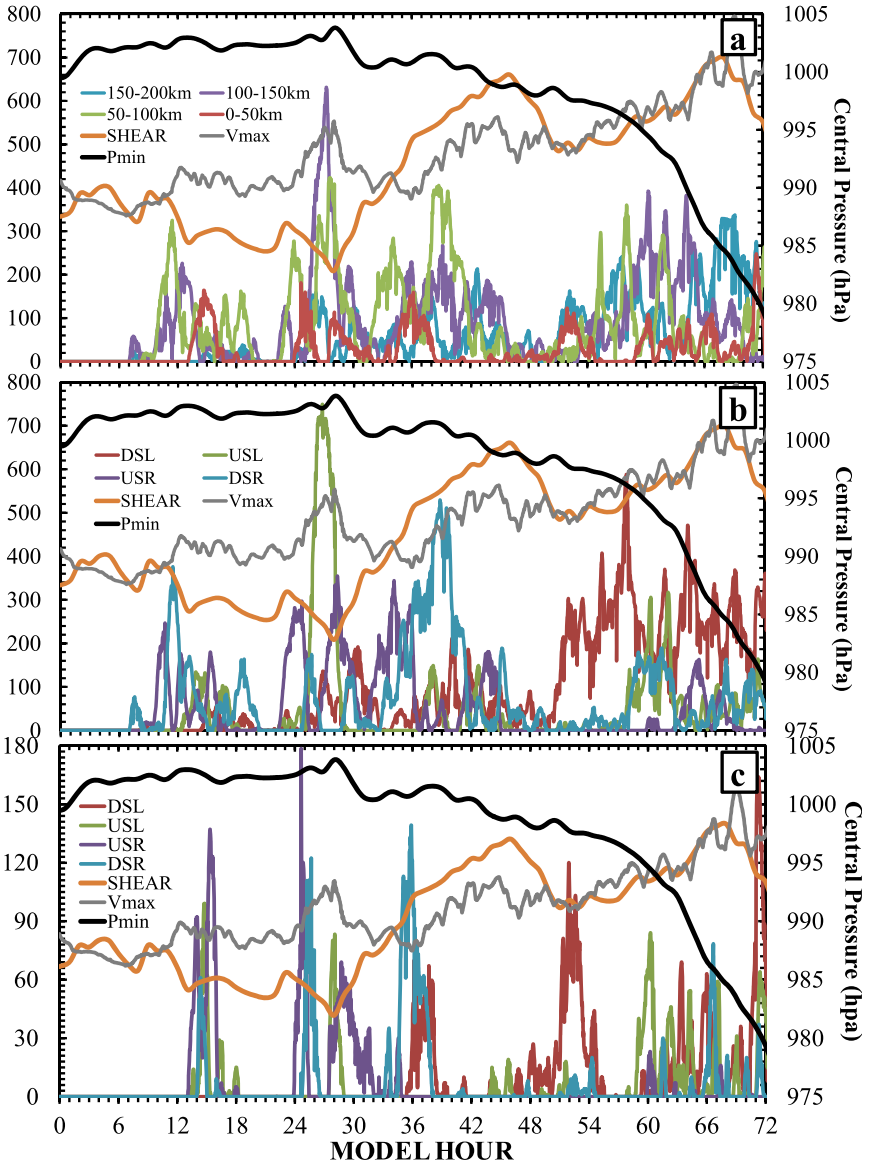

FIG. 7. Time series of 2-min resolution central pressure (black lines), shear magnitude (orange lines), maximum surface wind speed (gray lines) and (a) CB number stratified by radius $r \le 50$ km, $50 \le r \le 100$ km, $100 \le r \le 150$ km, and $150 \le r \le 200$ km (various colored lines); (b) as in (a), but with shear-oriented quadrants within a 200-km radius; and (c) as in (b), but with a 50-km radius for the first 72-h forecast. The shear magnitude is multiplied by 100 and the maximum surface wind is multiplied by 20 to fit the scale on the left axis for (a) and (b). The shear magnitude is multiplied by 20 and the maximum surface wind is multiplied by 4 to fit the scale on the left axis for (c).

To examine the relationship between subsidence in the inner core and intensity change, shear-oriented subsidence averaged from surface to 12-km altitude inside the 50-km radius is shown in Fig. 8. The subsidence in each quadrant between 24–39 h is quite vigorous, with multiple peaks up to 0.3 m s^{-1} that occur periodically, similar to the CBs in Fig. 7b. The subsidence in all quadrants is relatively weak between 39–50 h, after which there is sustained subsidence in the upshear-left quadrant. It appears from Figs. 7b and 8 that subsidence in the upshear-left quadrant is closely correlated in time to the CBs in the downshear-left quadrant. This is consistent with the results of Eastin et al. (2005b) and Reasor et al. (2009), which showed the subsidence is maximized in the upshear region next to the left-shear deep convection in Hurricane Guillermo (1997).

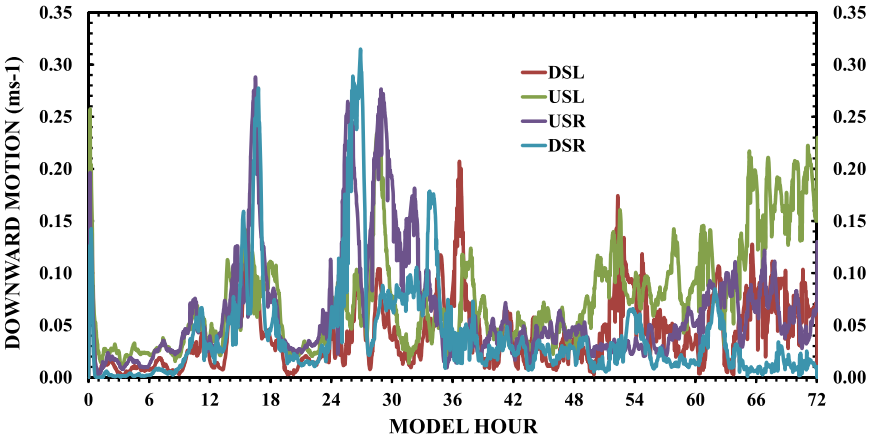

FIG. 8. Time series of subsidence (downward motion) averaged between 0 and 12 km within a 50-km radius for the first 72-h forecast for downshear left (DSL), upshear left (USL), upshear right (USR), and downshear right (DSR).

Figures 7 and 8 imply that RI onset is related to sustained convection in the downshear-left quadrant and subsidence in the upshear-left quadrant. To demonstrate how the downshear-left convection and upshear-left subsidence contribute to formation of the warm core and RI, Figs. 9a and 9c show the hourly averaged potential temperature anomaly (black contour) and vertical motion (shading) at 8-km altitude during RI preconditioning (i.e., 54–55 h) and RI onset (i.e., 57–58 h) stages, respectively. In Fig. 9a, the mesoscale vertical motion shows a wavenumber-1 asymmetry with ascent downshear and descent upshear. Superposed on this mesoscale vertical motion distribution is strong deep convection in the downshear-left quadrant and strong subsidence in the upshear-left quadrant next to downshear-left deep convection. The strongest subsidence is located along the downwind edge of deep convection. Associated with this distribution of vertical motion are two regions of warm anomaly—a broad one in the deep convection region with a maximum of 3 K and a narrow one in the subsidence region with a maximum of 2 K—separated by a cooling line (marked by a blue dashed line). The storm-relative circulation center at 8-km altitude ($\times$ in Fig. 9a) is located at the edge of downshear-left deep convection. This configuration allows flow at the upper level to advect the warm anomaly associated with subsidence in the upshear left toward the low-level storm center and reduce the surface pressure, which suggests the horizontal advection may play an important role in the development of the upper-level warm core. Stern and Zhang (2013a,b) also found that horizontal advection plays an important role in the formation of a warm-core structure, but at midlevels, which is different from this study. The hourly averaged diabatic heating distribution is very similar to the vertical motion distribution, with heating in the upward-motion area and cooling in the downward-motion area. Figure 9b shows the heating associated with deep convection in the downshear-left quadrant can be as large as 20 K h^{-1}, 95% of which is offset by the adiabatic cooling (not shown). Right next to the strong diabatic heating is strong evaporative cooling, which is up to 10 K hr^{-1} and is responsible for the cooling line seen in Fig. 9a. However, it is important to note that, despite a cooling trend due to microphysical processes at the downstream of the cooling line (Fig. 9a), it cannot offset the warming produced by subsidence farther downstream, resulting in net warming (Fig. 9a).

At 3 h later (Fig. 9c), the deep convection area has expanded significantly and is located farther northeast, with part of the deep convection occurring in the upshear-left quadrant. The warm anomaly region in the upshear left at this time becomes much more significant in terms of both coverage and magnitude compared to 3 h earlier. Figure 9d showed corresponding diabatic heating distribution, which is very similar to Fig. 9b, with strong diabatic heating associated with deep convection in the downshear left and evaporative cooling next to it responsible for the cooling line.

Figure 10 shows the azimuth–height cross section of vertical motion averaged between 50-km radius and 100-km radius during the preconditioning stage and RI onset. As it can be seen, all the deep convection concentrates in the downshear region, with most of it in the downshear left in the preconditioning stage (Fig. 10a). Compared to the upward motion, the downward motion shows more characteristics. There is a strong convective-scale downward motion labeled A downstream of deep convection in the downshear-left quadrant. Near the edge of deep convection and below the melting level, this convective-scale downward motion is greatly enhanced by the evaporation (labeled D). This distinct feature is

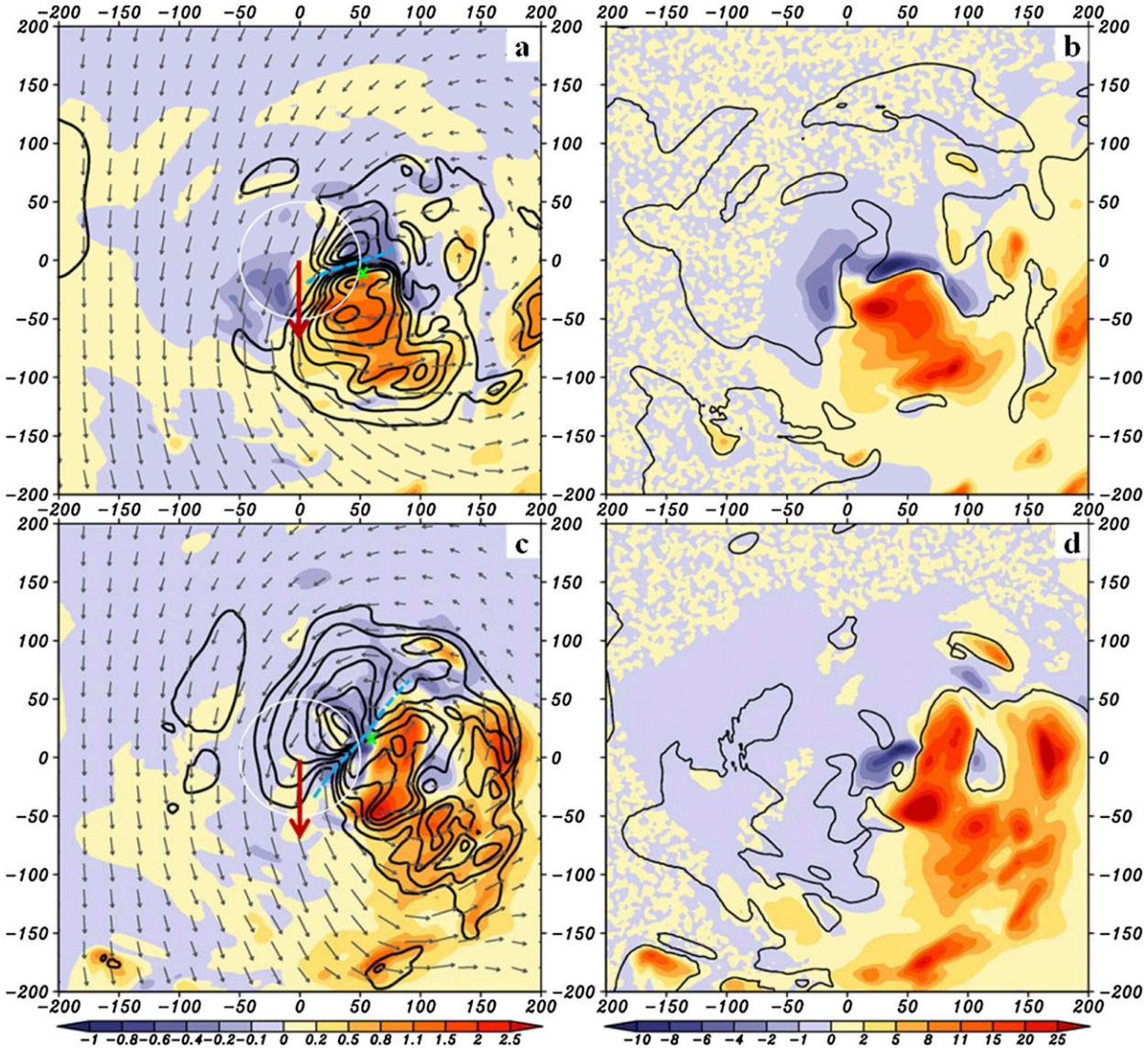

FIG. 9. (a),(c) Hourly averaged vertical motion (color shading, m s^{-1}) superposed with potential temperature anomaly (black contours at 0.5-K interval), shear vector (red arrows), and storm-relative flow vector (gray arrows) at 8-km altitude averaged between 54 and 55 h, corresponding to 0000–0100 UTC 29 Aug and between 57 and 58 h corresponding to 0300–0400 UTC 29 Aug, respectively. The white circle indicates the 50-km radius, and the blue dashed line indicates the cooling that separates diabatic heating from subsidence warming. The green cross indicates the circulation center at 8-km altitude. (b),(d) The hourly averaged diabatic heating (K h^{-1}) for 54–55 and 57–58 h, respectively. The black contours indicate zero vertical motion.

consistent with earlier studies of Liu et al. (1999). The strong evaporation-driven downward motion below the melting level also indicates that the cells have entered a mature stage. Also, the broad mesoscale subsidence in the upshear labeled B, which is the result of interaction between shear and vortex, occupies between 3 and 10 km at this time and is enhanced by the convective-scale subsidence at the downstream of deep convection. Higher up, there is another kind of subsidence labeled C, which results from the detrainment of stratospheric air because of the overshooting deep convection. This feature has also been documented by numerous studies (e.g., Velden and Smith 1983; Foley 1998). The detrainment subsidence seen in downshear left is unlikely to play a major role in the development of the upper-level warm core, since it will be advected away from the storm center by the upper-level circulation associated with the deep convection.

At 3 h later, the deep convection rotates cyclonically, and a small portion of deep convection occurs in the upshear left (Fig. 10b). The deep convection at this time

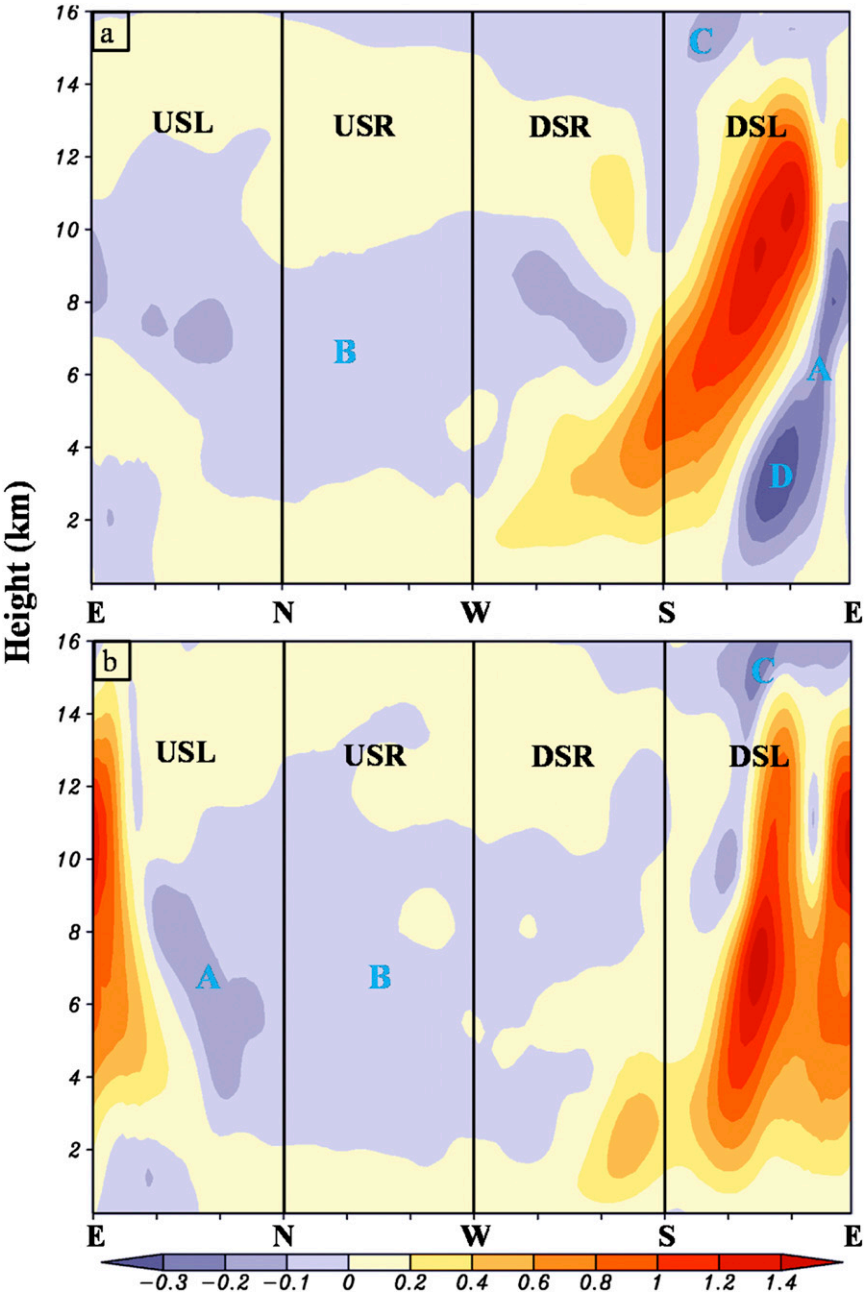

FIG. 10. Azimuth–height cross section of ring-averaged ($50 \leq r \leq 100$ km) vertical motion ($m\,s^{-1}$) and time averaged between (a) 54 and 55 and (b) 57 and 58 h. Blue letters A, B, C, and D indicate convective-scale downward motion, shear-driven mesoscale downward motion, stratospheric detrainment downward motion, and the section of downdraft enhanced by evaporation, respectively.

is more upright, in comparison with the slanted updraft in Fig. 10a. The lack of significant evaporation-driven downdraft below the melting level indicates that the convective cells are at their growing stages. Nevertheless, there is still convective-scale downward motion at the downstream of deep convection in the upshear-left quadrant (marked A in Fig. 10b). The broad mesoscale subsidence shown in Fig. 10a now extends vertically, occupying between 2 and 12 km. Higher up, the detrainment subsidence is still located at the upstream of deep convection, but it is stronger than 3 h earlier. This is consistent with the more upright deep convection at this time.

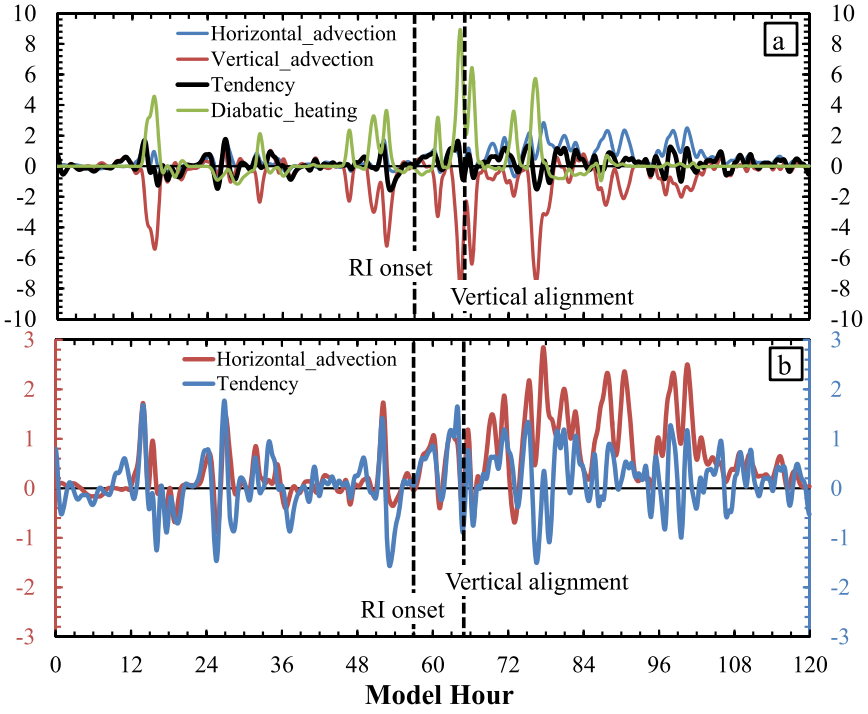

FIG. 11. (a) Time series of horizontal (blue line) and vertical (red line) advection of potential temperature, local tendency of potential temperature (black line), and diabatic heating associated with microphysics (green line) averaged over 8–14 km within a 15-km radius (K h^{-1}). (b) As in (a), but only horizontal advection of potential temperature (red line) and local tendency of potential temperature (blue line). Vertical black dashed lines indicate the timing of RI onset and vertical alignment.

To further examine the role of horizontal temperature advection in the development of the warm core, the averaged potential temperature energy budget was computed within the eye (i.e., radii $\leq$ 15 km) in the 8–14-km layer and is shown in Fig. 11. It should be emphasized that such a budget, especially for a real storm like Earl, may not be accurate because of the storm motion. Almost all the earlier works related to the thermodynamic budget computations have been restricted to nearly idealized, symmetric, and stationary storms (Stern and Zhang 2013a). In fact, we are in the process of producing idealized baseline experiments within the HWRF framework to compare the budgets for axisymmetric and symmetric intensification processes and evaluate the current results. Nevertheless, several interesting features may be isolated even within the current framework. Figure 11a shows the leading terms in the temperature budgets. Clearly, even within the radius of maximum wind, sporadic bursts take place. However, most of the heating is offset by vertical advection. In fact, even when there was some significant convection within the radius of maximum wind (Figs. 3d, 6a, and 7c), the residual between heating and vertical advection was still smaller than horizontal advection, very likely because these events were not persistent (Figs. 7a,c). Also, a closer look at the horizontal advection and local tendency (Fig. 11b) demonstrates that the former is very close to the local tendency in the pre-RI stage and almost identical to the local tendency in the period between RI onset and vertical alignment (i.e., 57–65 h). The warming due to horizontal advection results in the formation of a warm core in the upper troposphere (Figs. 6a and 9c). As discussed in the introductory section, this warm core will be supported by the evaporation and sensible heat supply from the warm ocean and inward enthalpy flux in the boundary layer. Furthermore, when the near-surface heat and moisture fluxes are transported upward by the mean secondary circulation, cumulus convection being the agent, a continual positive feedback is produced between the upward transport of near-surface fluxes, the deepening of pressure gradients primarily between the center and the eyewall, and the further increase in wind near the surface and deeper layer of the atmosphere (Gopalakrishnan et al. 2011). Later, during the intensification process (after about 78 h), when a better-defined eye develops, heating due to convective clouds in the eye has subsided. At this time, the net tendency is a balance between vertical and horizontal advection. Several past studies (Smith 1980; Willoughby 1998) have

all suggested subsidence as the primary mechanism for warming the eye, especially in matured-state hurricanes. Interestingly, our simulations indicate that Earl never reached that stage during the 120-h forecast. Even vertical alignment discussed here was only achieved relative to initial tilt (Figs. 4 and 5). Further examination shows, perhaps because of persistent shear (Fig. 2), Earl never achieves absolute vertical alignment, and the circulation displacement between 2 and 8 km is about 10 km even at the end of the 120-h forecast. Also, we noticed that this displacement wobbles between 10 and 25 km, even after vertical alignment. The slight tilt is the cause of the positive horizontal advection. The weak ascent might also be associated with the slight tilt, and this will be further examined in our future work.

7. Why does RI occur at that specific time?

We illustrated in section 6 that subsidence warming in the upshear-left quadrant is advected to the storm center and contributes to the development of an upper-level warm core. However, Fig. 7 shows that CBs occur almost all the time in the pre-RI stage and that they are even more vigorous between 24 and 42 h, yet RI occurs much later. Figure 7b provides a hint that persistent downshear-left dominance of CBs is the key. Why does the downshear-left region need to be dominant? What do CBs do in different quadrants?

It is well known that TCs that evolve in a sheared environment tend to produce organized convection in the downshear region and subsidence in the upshear region (e.g., Jones 1995). This scenario is also depicted in the forecast of Hurricane Earl by the HWRF system (Fig. 9). The process of RI in sheared storms may be viewed as a mechanism of cooperative interaction between large/mesoscale subsidence in the upshear region and subsidence produced by convective elements that form first in the downshear-left quadrant and then move cyclonically to the upshear quadrant, moistening the environment downstream near the low-level storm center. However, the scale, frequency, and, above all, location of these CBs appear to play a key role in the RI process. For the configuration to favor RI in a tilted vortex, it must allow for the maximum subsidence-induced warming to be advected over the low-level storm center.

To examine the difference between CBs occurring in the four shear-oriented quadrants, Fig. 12 shows the schematic configuration of convective-scale vertical motion and shear-induced mesoscale motion. The black arrow indicates shear direction. The light blue and red hemispheres denote the shear-induced mesoscale subsidence and ascent, respectively, which are weak but

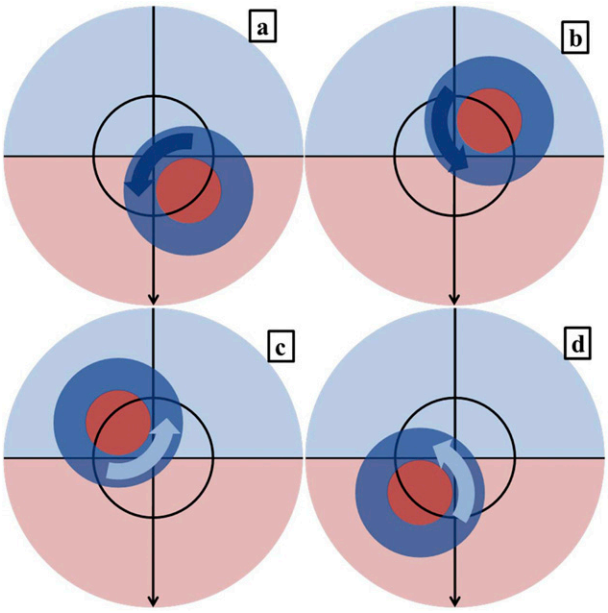

FIG. 12. Schematic depiction of configuration of shear-induced mesoscale subsidence (light blue semicircles), mesoscale ascent (light red semicircles), CBs (dark red circles), and convective-scale compensated subsidence (dark blue rings). The black circle indicates the RMW at the surface, and the black downward arrows show the shear direction (northerly shear). The thick blue curved arrows indicate the upper-level flow associated with CBs. For CBs located in (a) downshear left and (b) upshear left, convective-scale subsidence is superposed on the mesoscale subsidence. For CBs located in (c) upshear right and (d) downshear right, convective-scale subsidence is superposed on the mesoscale ascent.

balanced. The red circle indicates aggregated CBs, and the dark blue ring surrounding it shows the convective-scale subsidence. Compared to mesoscale vertical motion, the convective-scale vertical motion is strong but unbalanced. The thick blue arrow indicates the horizontal temperature advection associated with the net subsidence warming determined by mesoscale subsidence and convective-scale subsidence. The magnitude of advection is presented by the color of the arrow, with dark blue representing a larger magnitude. As can be seen, when CBs occur in the downshear-left and upshear-left quadrants (Figs. 12a,b), convective-scale subsidence induced at the downstream by the CBs is superposed on the mesoscale descent in the upshear region, and the net effect of the warming will be amplified, consistent with Reasor et al. (2009).

Compared to the favorable configuration just identified, upshear-right and downshear-right CBs produce subsidence in the mesoscale ascent region, which will offset the convective-scale subsidence warming and are not favorable for RI (Figs. 12c,d). The animation of horizontal temperature distribution indicates that the warming in the downshear region does not accumulate

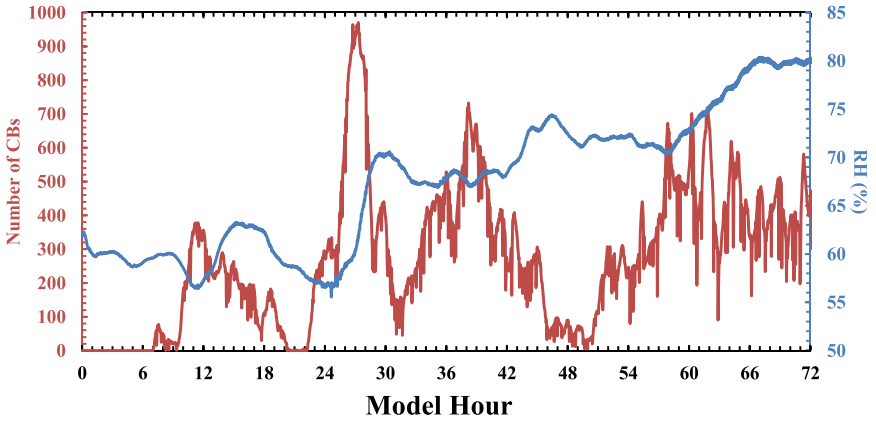

FIG. 13. Time series of the number of CBs (red) and domain-averaged relative humidity (blue) in 400 km × 400 km × 14 km.

(not shown); it only accumulates when sustained CB activity occurs in the downshear-left quadrant. This schematic figure also shows that the tilt magnitude–RMW configuration plays an important role. When the tilt is much larger than the surface RMW, the maximum warming may occur farther radially outward and will not be advected across the low-level storm center by the upper-level circulation to reduce the surface pressure in the most effective way.

The schematic image shown in Fig. 12 is depicted on the assumption that upper-level circulation is determined by the location of deep convection, which is the case when CBs are clustered in one quadrant instead of being scattering. For example, the vortex shows upshear tilt when most of the CBs occur in the upshear quadrants at 27 h. The tilt becomes southeastward when sustained downshear-left CBs dominate after 50 h. Zhang and Tao (2013) demonstrated that tilt is determined by deep convection when there is significant convection asymmetry. When CBs are scattered, each CB element competes with the others to become the new circulation center, and the upper-level circulation is disorganized. Hence, a cooperative configuration between mesoscale subsidence in the upshear region and organized convection is required for RI.

Although deep convection left of shear is shown to be more favorable for RI, random convective bursts do contribute to RI by moistening the vortex environment and allowing deep convection in the downshear-left quadrant to take place persistently. As shown in Fig. 13, the peak of relative humidity is a few hours later than the peak convective burst activity for each CB episode, suggesting convective bursts moisten the environment. After the first three convective burst episodes, which do not contribute to the development of upper-level warm core and RI directly, relative humidity increased from 60% to more than 70%. The moistened environment allows convection to take place in a more persistent way because of less entrainment, and upper-level circulation can develop. What drives these CB episodes is one of our future research topics.

8. Concluding remarks

- The asymmetric rapid intensification of a tropical cyclone, Hurricane Earl (2010), is simulated using the operational, ocean-coupled, HWRF system, and it is verified not only with best-track estimates, but also against inner-core observations, which were available especially during the preconditioning and RI stages of the storm.
- Apart from the routine track and 10-m wind speed, the model reproduced some salient, observed features of a sheared vortex, such as the asymmetric convective pattern and tilt of the storm both at the preconditioning and RI stages for the Earl case. The size prediction, in terms of the RMW, especially after the initial spinup process, was close to the observation. We believe that, in the absence of high-resolution observations in space and time, this forecast is useful in providing further insights on the RI process.
- Both the HWRF forecast and the observations indicate that strong convection is highly asymmetric in the preconditioning and RI stages, with most of the strong convection concentrated in the downshear and/or downshear-left quadrants. In contrast, the vertical vortex tilt evolves from the large tilt in the preconditioning and early RI stages to being almost vertically aligned in the later RI stage.
- The hourly hodograph of vortex tilt from the HWRF forecast reveals that the tilt is still large when RI starts at 57 h, and begins to decrease rapidly, suggesting that

the vertical alignment of the vortex is the result of RI rather than the trigger.

- Analysis of the 2-min HWRF forecast output shows that, despite the asymmetry in convective activities, RI onset is associated with a sudden warming in the upper troposphere above the 8-km altitude, without which RI would not have occurred, and the final pressure would be as much as 45 hPa higher.
- An in-depth analysis reveals that there are three stages associated with the RI of Earl: the preconditioning stage (i.e., 52–57 h), early RI stage (i.e., 57–65 h), and late RI stage (i.e., >65 h). In the preconditioning stage, most of the deep convection concentrates in the downshear-left quadrant, and a new circulation center develops at the upper level associated with the deep convection, which sets up the configuration for the cooperative interaction between the convective-scale subsidence and shear-induced mesoscale subsidence for the next stage. Nevertheless, random CBs in different quadrants prior to the preconditioning stage are found to moisten the environment near the vortex, and wind speed increases in response to these random CBs. Yet the wind speed only intensifies temporarily, without the warming having developed in the upper level as a result of CBs occurring in the optimum quadrants. In the early RI stage, the vortex is tilted, but the warming due to convective-scale subsidence and shear-induced mesoscale subsidence is advected toward the low-level storm center by the upper-level circulation. The asymmetric intensification process due to horizontal temperature advection at the upper level lowers the surface pressure effectively and initiates RI, while bringing the vortex to vertical alignment. In the late RI stage, the vortex is aligned, and the subsidence in the eye contributes to the symmetric intensification process.

It should be emphasized that, although cloud-resolving models show some promise in RI predictions for individual cases, there is much less skill in forecasting intensity with fidelity over several TC forecasts. Both storm-to-storm and cycle-to-cycle variability are not uncommon. For instance, while the overall predictions of the intensification for the Earl case were reasonable, even the subsequent forecast cycle produced a delayed intensification. Both uncertainties related to modeling boundary layer as well as microphysical processes may lead to uncertainties in forecasts. Thanks largely to some important in situ measurements, some improved understanding of the PBL processes has been attained in the recent times (e.g., Gopalakrishnan et al. 2012). However, a careful evaluation of modeled microphysics remains elusive to date. It is expected that some of the satellite observations may be helpful in reducing some of the forecast uncertainties in future.

Acknowledgments. The authors acknowledge funding from NOAA's Hurricane Forecast Improvement Program (HFIP), and this work was supported by NOAA Grants NA13OAR4830232 and NA14NWS4680028. We acknowledge the contributions from Drs. Thiago Quirino and Xuejin Zhang on the HWRF developmental efforts. Thanks are also due to Drs. Paul Reasor, Frank Marks, Robert Rogers, and Tomi Vukicevic for providing a thorough internal review and insightful comments that led to significant improvements of the original manuscript. Thanks are due to Ms. Gail Derr for offering editorial support and to Mr. Josh Alland, a summer intern, for analyzing some of the HWRF forecasts that led to this effort.

REFERENCES

Black, P. G., 1983: Ocean temperature changes induced by tropical cyclones. Ph.D. dissertation, The Pennsylvania State University, 278 pp. [Available from The Pennsylvania State University, University Park, PA 16802.]

Byers, H. R., 1944: *General Meteorology.* McGraw-Hill, 645 pp.

Cangialosi, J. P., 2010: Tropical cyclone report: Hurricane Earl, 25 August–4 September 2010. NOAA/NHC Tech. Rep. AL072010, 29 pp. [Available online at http://www.nhc.noaa.gov/pdf/TCR-AL072010_Earl.pdf.]

——, and J. L. Franklin, 2011: 2010 National Hurricane Center forecast verification report. NOAA/NHC Tech. Rep. 77 pp. [Available online at http://www.nhc.noaa.gov/verification/pdfs/Verification_2010.pdf.]

——, and ——, 2012: 2011 Atlantic and eastern North Pacific forecast verification. *Proc. 66th Interdepartmental Hurricane Conf.,* Charleston, SC, Office of the Federal Coordinator for Meteorology, 23 pp. [Available online at http://www.ofcm.gov/ihc12/Presentations/01b-Session/03-IHC_2012_Verification_(2012)_v2.pdf.]

Chen, H., 2012: On the rapid intensification of Hurricane Wilma (2005). Ph.D. dissertation, University of Maryland, 150 pp. [Available from Dept. of Atmospheric and Oceanic Science, University of Maryland, College Park, College Park, MD 20740.]

——, and D.-L. Zhang, 2013: On the rapid intensification of Hurricane Wilma (2005). Part II: Convective bursts and the upper-level warm core. *J. Atmos. Sci.,* **70,** 146–162, doi:10.1175/JAS-D-12-062.1.

——, ——, J. Carton, and R. Atlas, 2011: On the rapid intensification of Hurricane Wilma (2005). Part I: Model prediction and structural changes. *Wea. Forecasting,* **26,** 885–901, doi:10.1175/WAF-D-11-00001.1.

Chen, Q., and J. Fang, 2012: Effects of vertical wind shear on intensity and structure of tropical cyclone. *J. Trop. Meteor.,* **18,** 172–186.

Corbosiero, K. L., and J. Molinari, 2002: The effects of vertical wind shear on the distribution of convection in tropical cyclones. *Mon. Wea. Rev.,* **130,** 2110–2123, doi:10.1175/1520-0493(2002)130<2110:TEOVWS>2.0.CO;2.

——, and ——, 2003: The relationship between storm motion, vertical wind shear, and convective asymmetries in tropical cyclones. *J. Atmos. Sci.,* **60,** 366–376, doi:10.1175/1520-0469(2003)060<0366:TRBSMV>2.0.CO;2.

DeMaria, M., and J. Kaplan, 1994: Sea surface temperature and the maximum intensity of Atlantic tropical cyclones.

J. Climate, **7,** 1324–1334, doi:10.1175/1520-0442(1994)007<1324:SSTATM>2.0.CO;2.

Eastin, M. D., W. M. Gray, and P. G. Black, 2005a: Buoyancy of convective vertical motions in the inner core of intense hurricanes. Part I: General statistics. *Mon. Wea. Rev.,* **133,** 188–208, doi:10.1175/MWR-2848.1.

——, ——, and ——, 2005b: Buoyancy of convective vertical motions in the inner core of intense hurricanes. Part II: Case studies. *Mon. Wea. Rev.,* **133,** 209–227, doi:10.1175/MWR-2849.1.

Emanuel, K., 2003: A century of scientific progress: An evaluation. *Hurricane! Coping with Disaster: Progress and Challenges since Galveston 1900,* R. Simpson, R. Anthes, and M. Garstang, Eds., Amer. Geophys. Union, 177–204, doi:10.1029/SP055p0177.

Ferrier, B. S., 1994: A double-moment multiple-phase four-class bulk ice scheme. Part I: Description. *J. Atmos. Sci.,* **51,** 249–280, doi:10.1175/1520-0469(1994)051<0249:ADMMPF>2.0.CO;2.

Foley, G., 1998: A marked upper tropospheric temperature anomaly observed by an aircraft near a thunderstorm over inland western Australia. *Aust. Meteor. Mag.,* **47,** 321–326.

Frank, W. M., and E. A. Ritchie, 2001: Effects of vertical wind shear on the intensity and structure of numerically simulated hurricanes. *Mon. Wea. Rev.,* **129,** 2249–2269, doi:10.1175/1520-0493(2001)129<2249:EOVWSO>2.0.CO;2.

Gopalakrishnan, S. G., F. Marks, X. Zhang, J.-W. Bao, K.-S. Yeh, and R. Atlas, 2011: The experimental HWRF system: A study on the influence of horizontal resolution on the structure and intensity changes in tropical cyclones using an idealized framework. *Mon. Wea. Rev.,* **139,** 1762–1784, doi:10.1175/2010MWR3535.1.

——, and Coauthors, 2012: Hurricane Weather Research and Forecasting (HWRF) Model: 2012 scientific documentation. HWRF Development Testbed Center Tech. Rep. 96 pp. [Available online at: http://www.dtcenter.org/HurrWRF/users/docs/scientific_documents/HWRFScientificDocumentation_v3.4a.pdf.]

——, F. Marks, J. A. Zhang, X. Zhang, J.-W. Bao, and V. Tallapragada, 2013: A study of the impacts of vertical diffusion on the structure and intensity of the tropical cyclones using the high-resolution HWRF system. *J. Atmos. Sci.,* **70,** 524–541, doi:10.1175/JAS-D-11-0340.1.

Gray, W. M., 1968: Global view of the origin of tropical disturbances and storms. *Mon. Wea. Rev.,* **96,** 669–700, doi:10.1175/1520-0493(1968)096<0669:GVOTOO>2.0.CO;2.

Guimond, S. R., G. M. Heymsfield, and F. J. Turk, 2010: Multiscale observations of Hurricane Dennis (2005): The effects of hot towers on rapid intensification. *J. Atmos. Sci.,* **67,** 633–654, doi:10.1175/2009JAS3119.1.

Hack, J. J., and W. H. Schubert, 1986: Nonlinear response of atmospheric vortices to heating by organized cumulus convection. *J. Atmos. Sci.,* **43,** 1559–1573, doi:10.1175/1520-0469(1986)043<1559:NROAVT>2.0.CO;2.

Harnos, D. S., and S. W. Nesbitt, 2011: Convective structure in rapidly intensifying tropical cyclones as depicted by passive microwave measurements. *Geophys. Res. Lett.,* **38,** L07805, doi:10.1029/2011GL047010.

Hendricks, E. A., M. T. Montgomery, and C. A. Davis, 2004: The role of ''vortical'' hot towers in the formation of Tropical Cyclone Diana (1984). *J. Atmos. Sci.,* **61,** 1209–1232, doi:10.1175/1520-0469(2004)061<1209:TROVHT>2.0.CO;2.

Heymsfield, G. M., J. B. Halverson, J. Simpson, L. Tian, and T. P. Bui, 2001: ER-2 Doppler radar investigations of the eyewall of Hurricane Bonnie during the Convection and Moisture Experiment-3. *J. Appl. Meteor.,* **40,** 1310–1330, doi:10.1175/1520-0450(2001)040<1310:EDRIOT>2.0.CO;2.

Hong, S.-Y., and H.-L. Pan, 1996: Nonlocal boundary layer vertical diffusion in a Medium-Range Forecast Model. *Mon. Wea. Rev.,* **124,** 2322–2339, doi:10.1175/1520-0493(1996)124<2322:NBLVDI>2.0.CO;2.

Jiang, H., 2012: The relationship between tropical cyclone intensity change and the strength of inner-core convection. *Mon. Wea. Rev.,* **140,** 1164–1176, doi:10.1175/MWR-D-11-00134.1.

Jones, S. C., 1995: The evolution of vortices in vertical shear. I: Initially barotropic vortices. *Quart. J. Roy. Meteor. Soc.,* **121,** 821–851, doi:10.1002/qj.49712152406.

Kaplan, J., and M. DeMaria, 2003: Large-scale characteristics of rapidly intensifying tropical cyclones in the North Atlantic basin. *Wea. Forecasting,* **18,** 1093–1108, doi:10.1175/1520-0434(2003)018<1093:LCORIT>2.0.CO;2.

——, ——, and J. A. Knaff, 2010: A revised tropical cyclone rapid intensification index for the Atlantic and eastern North Pacific basins. *Wea. Forecasting,* **25,** 220–241, doi:10.1175/2009WAF2222280.1.

Kieper, M., and H. Jiang, 2012: Predicting tropical cyclone rapid intensification using the 37 GHz ring pattern identified from passive microwave measurements. *Geophys. Res. Lett.,* **39,** L13804, doi:10.1029/2012GL052115.

Kossin, J., and W. H. Schubert, 2001: Mesovortices, polygonal flow patterns, and rapid pressure falls in hurricane-like vortices. *J. Atmos. Sci.,* **58,** 2196–2209, doi:10.1175/1520-0469(2001)058<2196:MPFPAR>2.0.CO;2.

Liu, Q., N. Surgi, S. Lord, W.-S. Wu, D. Parrish, S. Gopalakrishnan, J. Waldrop, and J. Gamache, 2006: Hurricane initialization in HWRF model. *27th Conf. on Hurricanes and Tropical Meteorology,* Monterey, CA, Amer. Meteor. Soc., 8A.2. [Available online at https://ams.confex.com/ams/27Hurricanes/techprogram/paper_108496.htm.]

Liu, Y., D.-L. Zhang, and M. K. Yau, 1999: A multiscale numerical study of Hurricane Andrew (1992). Part II: Kinematics and inner-core structures. *Mon. Wea. Rev.,* **127,** 2597–2616, doi:10.1175/1520-0493(1999)127<2597:AMNSOH>2.0.CO;2.

Marks, F. D., 1985: Evolution of the structure of precipitation in Hurricane Allen (1980). *Mon. Wea. Rev.,* **113,** 909–930, doi:10.1175/1520-0493(1985)113<0909:EOTSOP>2.0.CO;2.

Merrill, R. T., 1988: Environmental influences on hurricane intensification. *J. Atmos. Sci.,* **45,** 1678–1687, doi:10.1175/1520-0469(1988)045<1678:EIOHI>2.0.CO;2.

Molinari, J., and D. Vollaro, 2010: Rapid intensification of a sheared tropical storm. *Mon. Wea. Rev.,* **138,** 3869–3885, doi:10.1175/2010MWR3378.1.

——, P. Dodge, D. Vollaro, K. L. Corbosiero, and F. Marks, 2006: Mesoscale aspects of the downshear reformation of a tropical cyclone. *J. Atmos. Sci.,* **63,** 341–354, doi:10.1175/JAS3591.1.

Montgomery, M. T., M. E. Nicholls, T. A. Cram, and A. B. Saunders, 2006: A vortical hot tower route to tropical cyclogenesis. *J. Atmos. Sci.,* **63,** 355–386, doi:10.1175/JAS3604.1.

——, J. A. Zhang, and R. K. Smith, 2014: An analysis of the observed low-level structure of rapidly intensifying and mature hurricane Earl (2010). *Quart. J. Roy. Meteor. Soc.,* **140,** 2132–2146, doi:10.1002/qj.2283.

Nguyen, M. C., M. J. Reeder, N. E. Davidson, R. K. Smith, and M. T. Montgomery, 2011: Inner-core vacillation cycles during the intensification of Hurricane Katrina. *Quart. J. Roy. Meteor. Soc.,* **137,** 829–844, doi:10.1002/qj.823.

Nolan, D. S., Y. Moon, and D. P. Stern, 2007: Tropical cyclone intensification from asymmetric convection: Energetics and efficiency. *J. Atmos. Sci.,* **64,** 3377–3405, doi:10.1175/JAS3988.1.

Reasor, P., and M. D. Eastin, 2012: Rapidly intensifying Hurricane Guillermo (1997). Part II: Resilience in shear. *Mon. Wea. Rev.,* **140,** 425–444, doi:10.1175/MWR-D-11-00080.1.

——, M. T. Montgomery, and L. D. Grasso, 2004: A new look at the problem of tropical cyclones in vertical shear flow: Vortex resiliency. *J. Atmos. Sci.,* **61,** 3–22, doi:10.1175/1520-0469(2004)061<0003:ANLATP>2.0.CO;2.

——, M. D. Eastin, and J. F. Gamache, 2009: Rapidly intensifying Hurricane Guillermo (1997). Part I: Low-wavenumber structure and evolution. *Mon. Wea. Rev.,* **137,** 603–631, doi:10.1175/2008MWR2487.1.

Riemer, M., M. T. Montgomery, and M. E. Nicholls, 2010: A new paradigm for intensity modification of tropical cyclones: Thermodynamic impact of vertical wind shear on the inflow layer. *Atmos. Chem. Phys.,* **10,** 3163–3188, doi:10.5194/acp-10-3163-2010.

Rodgers, E. B., W. S. Olson, V. M. Karyampudi, and H. F. Pierce, 1998: Satellite-derived latent heating distribution and environmental influences in Hurricane Opal (1995). *Mon. Wea. Rev.,* **126,** 1229–1247, doi:10.1175/1520-0493(1998)126<1229:SDLHDA>2.0.CO;2.

Rogers, R. F., S. Lorsolo, P. Reasor, J. Gamache, and F. Marks, 2012: Multiscale analysis of tropical cyclone kinematic structure from airborne Doppler radar composites. *Mon. Wea. Rev.,* **140,** 77–99, doi:10.1175/MWR-D-10-05075.1.

——, P. Reasor, and S. Lorsolo, 2013: Airborne Doppler observations of the inner-core structural differences between intensifying and steady-state tropical cyclones. *Mon. Wea. Rev.,* **141,** 2970–2991, doi:10.1175/MWR-D-12-00357.1.

——, ——, and J. A. Zhang, 2015: Multiscale structure and evolution of Hurricane Earl (2010) during rapid intensification. *Mon. Wea. Rev.,* doi:10.1175/MWR-D-14-00175.1, in press.

Schubert, W. H., and J. J. Hack, 1982: Inertial stability and tropical cyclone development. *J. Atmos. Sci.,* **39,** 1687–1697, doi:10.1175/1520-0469(1982)039<1687:ISATCD>2.0.CO;2.

Shay, L. K., G. J. Goni, and P. G. Black, 2000: Effects of a warm oceanic feature on Hurricane Opal. *Mon. Wea. Rev.,* **128,** 1366–1383, doi:10.1175/1520-0493(2000)128<1366:EOAWOF>2.0.CO;2.

Sitkowski, M., and G. M. Barnes, 2009: Low-level thermodynamic, kinematic, and reflectivity fields of Hurricane Guillermo (1997) during rapid intensification. *Mon. Wea. Rev.,* **137,** 645–663, doi:10.1175/2008MWR2531.1.

Smith, R. K., 1980: Tropical cyclone eye dynamics. *J. Atmos. Sci.,* **37,** 1227–1232, doi:10.1175/1520-0469(1980)037<1227:TCED>2.0.CO;2.

Steranka, J., E. B. Rodgers, and R. C. Gentry, 1986: The relationship between satellite-measured convective bursts and tropical cyclone intensification. *Mon. Wea. Rev.,* **114,** 1539–1546, doi:10.1175/1520-0493(1986)114<1539:TRBSMC>2.0.CO;2.

Stern, D. P., and F. Zhang, 2013a: How does the eye warm? Part I: A potential temperature budget analysis of an idealized tropical cyclone. *J. Atmos. Sci.,* **70,** 73–90, doi:10.1175/JAS-D-11-0329.1.

——, and ——, 2013b: How does the eye warm? Part II: Sensitivity to vertical wind shear and a trajectory analysis. *J. Atmos. Sci.,* **70,** 1849–1873, doi:10.1175/JAS-D-12-0258.1.

Tallapragada, V., C. Kieu, Y. Kwon, S. Trahan, Q. Liu, Z. Zhang, and I.-H. Kwon, 2014: Evaluation of storm structure from the operational HWRF during 2012 implementation. *Mon. Wea. Rev.,* **142,** 4308–4325, doi:10.1175/MWR-D-13-00010.1.

Tang, B., and K. Emanuel, 2010: Midlevel ventilation's constraint on tropical cyclone intensity. *J. Atmos. Sci.,* **67,** 1817–1830, doi:10.1175/2010JAS3318.1.

Van Sang, N., R. K. Smith, and M. T. Montgomery, 2008: Tropical-cyclone intensification and predictability in three dimensions. *Quart. J. Roy. Meteor. Soc.,* **134,** 563–582, doi:10.1002/qj.235.

Velden, C. S., and W. L. Smith, 1983: Monitoring tropical cyclone evolution with NOAA satellite microwave observations. *J. Climate Appl. Meteor.,* **22,** 714–724, doi:10.1175/1520-0450(1983)022<0714:MTCEWN>2.0.CO;2.

Vigh, J. L., and W. H. Schubert, 2009: Rapid development of the tropical cyclone warm core. *J. Atmos. Sci.,* **66,** 3335–3350, doi:10.1175/2009JAS3092.1.

Willoughby, H. E., 1998: Tropical cyclone eye thermodynamics. *Mon. Wea. Rev.,* **126,** 3053–3067, doi:10.1175/1520-0493(1998)126<3053:TCET>2.0.CO;2.

——, J. A. Clos, and M. G. Shoreibah, 1982: Concentric eye walls, secondary wind maxima, and the evolution of the hurricane vortex. *J. Atmos. Sci.,* **39,** 395–411, doi:10.1175/1520-0469(1982)039<0395:CEWSWM>2.0.CO;2.

Yablonsky, R. M., and I. Ginis, 2008: Improving the ocean initialization of coupled hurricane–ocean models using feature-based data assimilation. *Mon. Wea. Rev.,* **136,** 2592–2607, doi:10.1175/2007MWR2166.1.

Zhang, D.-L., and H. Chen, 2012: Importance of the upper-level warm core in the rapid intensification of a tropical cyclone. *Geophys. Res. Lett.,* **39,** L02806, doi:10.1029/2011GL050578.

Zhang, F., and D. Tao, 2013: Effects of vertical wind shear on the predictability of tropical cyclones. *J. Atmos. Sci.,* **70,** 975–983, doi:10.1175/JAS-D-12-0133.1.

Zhang, J. A., R. Rogers, P. Reasor, E. W. Uhlhorn, and F. D. Marks, 2013: Asymmetric hurricane boundary layer structure from dropsonde composites in relation to the environmental vertical wind shear. *Mon. Wea. Rev.,* **141,** 3968–3984, doi:10.1175/MWR-D-12-00335.1.